




The Effects of Hydroxyapatite Addition on the Properties of the Mechanically Alloyed and Sintered Mg-RE-Zr Alloy

K. Kowalski , M. Nowak, J. Jakubowicz, and M. Jurczyk

(Submitted January 29, 2016; published online August 31, 2016)

This paper discusses the influence of the chemical composition on the microstructure, mechanical and corrosion properties of mechanically alloyed and sintered (Mg-4Y-5.5Dy-0.5Zr)-*x* wt.% HA composites. Mechanical alloying for 25 h of the Mg-4Y-5.5Dy-0.5Zr composition, followed by sintering under argon at 550 °C for 2 h, led to the formation of a bulk alloy with an ultrafine grained microstructure. With the increase of the hydroxyapatite content in the (Mg-4Y-5.5Dy-0.5Zr)-*x* wt.% HA composite, a reduction of the grain sizes of the bulk material was noticeable. In the case of the bulk (Mg-4Y-5.5Dy-0.5Zr)-10 wt.% HA composite, the grain sizes of approx. 60 nm have been recorded by atomic force microscopy. The final microstructure of the synthesized composites strongly influenced the mechanical and corrosion properties. The Mg-4Y-5.5Dy-0.5Zr alloy was characterized by higher average values of Young's modulus (36.6 GPa). In the case of the (Mg-4Y-5.5Dy-0.5Zr)-5 wt.% HA scaffolds with the porosity of 48%, the Young's modulus was equal to 7.1 GPa. The (Mg-4Y-5.5Dy-0.5Zr)-10 wt.% HA composite was more corrosion resistant ($I_c = 5.849 \times 10^{-5} \text{ A cm}^{-2}$, $E_c = -1.565 \text{ V}$ versus SCE) than Mg-4Y-5.5Dy-0.5Zr alloy ($I_c = 4.838 \times 10^{-4} \text{ A cm}^{-2}$, $E_c = -1.555 \text{ V}$ versus SCE). The influence of hydrofluoric acid treatment on the corrosion behavior of the (Mg-4Y-5.5Dy-0.5Zr)-5 wt.% HA composite was also investigated. The electrochemical test showed that the corrosion resistance of fluoride-treated specimens was higher, compared with the untreated samples in the Ringer's solution. In conclusion, fluoride-treated (Mg-4Y-5.5Dy-0.5Zr)-HA composites are biodegradable materials with adjustable mechanical and corrosive properties.

Keywords hydroxyapatite, mechanical alloying, mechanical characterization, magnesium alloys, metallic matrix composites, rare earth, x-ray diffraction

1. Introduction

Ultrafine- or nanocrystalline Mg-based alloys produced by the application of non-equilibrium processing techniques, such as equal channel angular pressing (ECAP), rapid solidification (RS) or mechanical alloying (MA), demonstrate novel properties compared to conventional (microcrystalline) materials (Ref 1-3). Mechanical alloying is a powder processing technique that enables the production of nanomaterials starting from mixed elemental powders in the right proportion followed by loading the powder mixture into the mill along with the milling balls. The milled nanocrystalline powders are finally compacted and heat-treated to obtain the desired microstructure and properties (Ref 1, 4). Recent studies have clearly demonstrated that the nanostructuring of metallic biomaterials can considerably improve not only its mechanical properties but also its biocompatibility (Ref 5, 6).

Magnesium and its alloys have attracted a lot of attention as potential bone implant materials. They are characterized by non-toxicity, outstanding biological performance and biodegradability in physiological environment (Ref 3, 7, 8).

However, high reactivity and poor corrosion resistance in chloride-containing solutions, including human body fluid, are a disadvantage (Ref 3). The poor corrosion resistance depends on: (1) impurities and/or secondary phases and (2) the quality of the oxide films on the Mg surface (Ref 3, 9, 10).

Magnesium is usually alloyed with other metals. The alloying elements have been studied for developing biodegradable Mg-type alloys with good mechanical and corrosion properties. Three groups of magnesium alloys can be distinguished (Ref 3, 11): (1) alloys containing Mn, Zn (Mg-Mn-Zn), (2) alloys containing Zn, RE (Rare Earth), Y, Zr, Th (Mg-Zn-Zr, Mg-Zn-RE, Mg-Y-RE-Zr (WE43), Mg-Th and (3) new ultralight alloys containing Li (Mg-Li-Al). For good biocompatibility of Mn and Zn, they were selected as the alloying elements to develop Mg-Mn-Zn alloys. The addition of these metals improves not only the mechanical properties but also the corrosion resistance of magnesium alloys.

In the presence of a multiphase structure, magnesium alloys undergo a localized corrosion due to galvanic effects, and therefore the formation of less cathodic intermetallic compounds can explain the higher corrosion resistance exhibited by the Mg-RE alloys (Ref 12). Commercial WE43 magnesium alloy has a nominal composition of Mg-(3.7-4.4)Y-(2.3-3.5RE; rare earth)-0.2 Zr (Ref 13). Their desirable combination of relatively good tensile properties and high-temperature creep resistance are associated with densely distributed precipitates (Ref 14).

Enhanced mechanical properties have been reported in Mg composites reinforced with nanoscaled ceramic particles such as hydroxyapatite (HA, $\text{Ca}_{10}(\text{PO}_4)_6(\text{OH})_2$) (Ref 15, 16). HA is chemically similar to the mineral component of bones and hard tissues in mammals. Moreover, it possesses the capacity to integrate in bone structures and support bone ingrowth, without

K. Kowalski, M. Nowak, J. Jakubowicz, and M. Jurczyk, Institute of Materials Science and Engineering, Poznan University of Technology, Jana Pawla II 24, 61-139 Poznan, Poland. Contact e-mail: kamil.kowalski@put.poznan.pl.

breaking down or dissolving. Dense HA, however, does not have the mechanical strength to ensure long-term load-bearing applications. Coatings of hydroxyapatite are often applied to metallic implants (titanium, titanium alloys and stainless steels) to modify the surface properties, but in many cases satisfactory results are not achieved, due to crack formation or badly controlled adjustment of the specific apatite phases. Latest studies have focused on the possibility of its application in composite form, in materials combining metal with bioceramic (Ref 3, 15-19). These studies aim at optimizing the mechanical properties of the composites.

The mechanical alloying method and the powder metallurgy process have been developed for the fabrication of bulk Ti-HA and Ni-free austenitic stainless steel-HA nanocomposites with a unique microstructure (Ref 3, 17). Independently, metal matrix composites (MMC) composed of magnesium alloy AZ91D as a matrix and hydroxyapatite particles as reinforcements have been examined in vitro for mechanical, corrosive and cytocompatible properties (Ref 18). The mechanical properties of the MMC-HA were dependent on the HA particle size and distribution.

To date, the effect of nanohydroxyapatite contents (0-10 wt.%) on the microstructure and mechanical properties of magnesium nanocomposites densified by high frequency induction heat sintering has been investigated (Ref 15). The relative density and microhardness of the sintered samples reached as high as 99.7% and 70 HV, respectively, in the composite containing 1-3 wt.% HA. The addition of 1-3 wt.% of HA improved the compression strength of Mg by 16%. Due to the agglomeration of HA particles, the compressive strength decreased when the HA content was larger than 2 wt.%. A uniform distribution of HA particles was observed along the boundary between the Mg-matrix particles.

Recently, an open-porous, mechanically adaptable metal scaffold made of W4 magnesium alloy melt-extracted short fibers was fabricated by liquid-phase sintering (Ref 20). A pilot in vivo study for 6 and 12 weeks demonstrated active bone remodeling, no foreign object reaction and no clinical observation of gas formation during W4 scaffold implantation. Additionally, the effect of porosity was studied on the corrosion resistance of MRI 201S magnesium alloy foams in 0.9% NaCl solution and in phosphate buffer saline solution as a simulated physiological electrolyte. The porosity in the range of 14-19% can increase the corrosion rate of this alloy by more than one order of magnitude compared to its corrosion rate in cast conditions.

The present study examines the microstructure, mechanical and corrosion properties of the sintered Mg-4Y-5.5Dy-0.5Zr alloy through hydroxyapatite alloying. The influence of the hydrofluoric acid (HF) treatment on the corrosion behavior of synthesized nanocomposites was studied. The properties of (Mg-4Y-5.5Dy-0.5Zr)- x wt.% HA composites with ultrafine grains as well as nanograins and its scaffolds have not been previously investigated ($0 \leq x \leq 10$). The authors hope that the obtained results will offer a guide for further studies and development of Mg-based composites with better properties.

2. Materials and Methods

The present work contains the results of a research carried out for the (Mg-4Y-5.5Dy-0.5Zr)- x wt.% HA composites.

These materials were prepared by the MA and powder metallurgy. Elemental powders of magnesium (99.8% purity, maximum particle size 45 μm ; Alfa Aesar), zirconium (95.0% purity, maximum particle size 350 μm ; Ciech-Poland) and hydroxyapatite (reagent grade; Sigma-Aldrich) were used as the starting materials. Powders of yttrium and dysprosium (about 100 μm in size) were made from the bulk samples (99.9% purity; Alfa Aesar) by filing in the argon atmosphere. The elemental powders were weighed, blended and poured into a round bottom stainless vial in a glove box (Labmaster 130) filled with automatically controlled argon atmosphere ($\text{O}_2 \leq 2$ ppm and $\text{H}_2\text{O} \leq 1$ ppm) to obtain the nominal composition (Mg-4Y-5.5Dy-0.5Zr)- x wt.% HA.

Mechanical alloying was carried out using a SPEX mixer mill (model 8000), employing a BPR of 20:1 at ambient temperature for 25 h in a continuous mode. The bulk (Mg-4Y-5.5Dy-0.5Zr)- x wt.% HA composites and their scaffolds were prepared using the powder metallurgy. In the first case, the powders were uniaxially pressed at a compacting pressure of 600 MPa. The typical dimensions of the pellets were $d = 8$ mm in diameter and $h = 3$ mm in height. Finally, the green compacts were heat-treated at 550 $^\circ\text{C}$ for 2 h under argon (99.999% purity) to form bulk samples. In the second case, the blended (Mg-4Y-5.5Dy-0.5Zr)- x wt.% HA was mixed with ammonium hydrogen carbonate (NH_4HCO_3) that was used as the space-holder material. The size of the space-holder particles was 500-800 μm . The mixture containing the mechanically alloyed (Mg-4Y-5.5Dy-0.5Zr)-5 wt.% HA powder and NH_4HCO_3 was uniaxially pressed at a compacting pressure of 400 MPa. The resulting pellets were typically 8 mm in diameter and 5 mm in height. The green compacts were sintered under a vacuum of 10^{-4} Torr in two steps. The first step was conducted at 175 $^\circ\text{C}$ for 2 h to remove the space-holder particles. In the second step, the compacts were heat-treated at 550 $^\circ\text{C}$ for 2 h for sintering. The porous (Mg-4Y-5.5Dy-0.5Zr)-5 wt.% HA composites with the porosity of 48% were fabricated by adding 30 wt.% ammonium hydrogen carbonate to the powder mixture.

For all tests, the disks of bulk (Mg-4Y-5.5Dy-0.5Zr)- x wt.% HA composites, (Mg-4Y-5.5Dy-0.5Zr)-5 wt.% HA scaffolds and microcrystalline Mg (prepared from a commercial Mg cylinder with a diameter of 8 mm by slicing into disks with a thickness of 3 mm; Alfa Aesar) were grinded with 1000 grit SiC paper in water and ultrasonically rinsed with acetone.

The crystallographic structure of the samples during different processing stages was investigated at a room temperature using a Panalytical Empyrean x-ray diffraction (XRD) with $\text{CuK}\alpha$ ($\lambda = 1.54056$ \AA) radiation. The crystal size (d) and the internal strain (ϵ) were calculated from the Mg (101) diffraction peak position.

The microstructure of bulk-synthesized materials was studied with the use of the Quesant Q-Scope 250TM atomic force microscope (AFM). In these studies, phase contrast imaging provided the best results in terms of distinguishing of microstructural elements of the material. The NanoAndMore GmbH pre-mounted SuperSharpSilicon NanosensorsTM probe with tip radius of 2 nm and a resonant frequency of approx. 140 kHz was applied for the surface scanning in the tapping mode. The scanning procedure was done with the scan rate of 3 Hz (3 lines/s; total 1024 lines per image). The authors used an AFM piezoelectric scanner with the maximum scan size of 48 μm . The AFM microscope was isolated from the environment using the antivibrating chamber. Based on the AFM

images, the particle size dimension distribution histograms were made. The microstructure, morphology of crystallite agglomerates and elements composition of the obtained powders were determined by scanning electron microscopy (SEM) (Tescan model Vega 5135) associated with energy dispersive spectroscopy (EDS) (GT model Prism 200 Avalon).

The densities of the sintered samples were determined using the Archimedes method. The porosity of the porous materials was calculated by the formula $\rho = (1 - \rho/\rho_{th}) \times 100\%$, where ρ and ρ_{th} are the density of the porous material and its corresponding theoretical density (calculated for the rule of mixtures), respectively.

The Vickers microhardness of the bulk samples was measured using a microhardness tester by applying a load of 300 g on the polished surfaces of the samples. For each sample, 10 separate indents were created on the investigated surface. For the evaluation of the Young's modulus of bulk and porous Mg-based composites, tensile tests were performed at room temperature using a universal material testing machine operating under a strain rate of 10^{-3} s^{-1} . The tensile test specimen was in accordance with the subsize ASTM E-8 standard.

The corrosion resistance of different samples was measured in the Ringer's solution (simulated body fluid (SBF) containing aggressive chloride, of the following composition: NaCl 9 g/l, KCl 0.42 g/l, CaCl₂ 0.48 g/l, NaHCO₃ 0.2 g/l), applying potentiodynamic mode with the scan rate of 0.5 mV/s at temperature of $37 \pm 1 \text{ }^\circ\text{C}$, controlled by thermostat. The Solartron 1285 potentiostat was applied. The corrosion test was run in the EG&G K0047 corrosion cell. The counter electrode consisted of two graphite rods, and a saturated calomel electrode (SCE) was used as the reference electrode. The surface area exposed to the electrolyte was 0.8 mm^2 . The corrosion potentials (E_c) and corrosion current densities (I_c) were estimated from the Tafel extrapolations of the polarization curves, using CorrView software.

For surface HF treatment, the polished samples were washed with distilled water, rinsed and ultrasonically degreased with ethanol and dried in air. Then, the specimens were immersed in 40% hydrofluoric acid for 2 h at a room temperature. Finally, the samples were washed with deionized water, dried and subsequently assessed visually for the uniformity of surface layer.

3. Results

The evolution of crystallographic structure during mechanical milling has been studied. Figure 1 shows XRD patterns from the mechanically alloyed (Mg-4Y-5.5Dy-0.5Zr)-5 wt.% HA as a representative composite example after different milling times. Mg has an hcp structure (CAS Number: 7439-95-4) with the lattice parameters of $a = 3.210 \text{ \AA}$, $c = 5.211 \text{ \AA}$ (P6₃/mmc space group). In the Mg-4Y-5.5Dy-0.5Zr composition, the Y, Dy, Zr peaks disappeared completely for the sample milled for 5 min (Fig. 1a). By increasing the milling time, the characteristic peak of Mg (101) was shifted to a lower diffraction angle due to the dissolution of Y, Dy and Zr in the Mg matrix. Figure 2 illustrates the variation of the "a" and "c" lattice parameters in the Mg-4Y-5.5Dy-0.5Zr sample during milling. The Mg phase suffers an important increase of both parameters. An ultrafine phase with a hexagonal structure similar to that of Mg forms after 25 h.

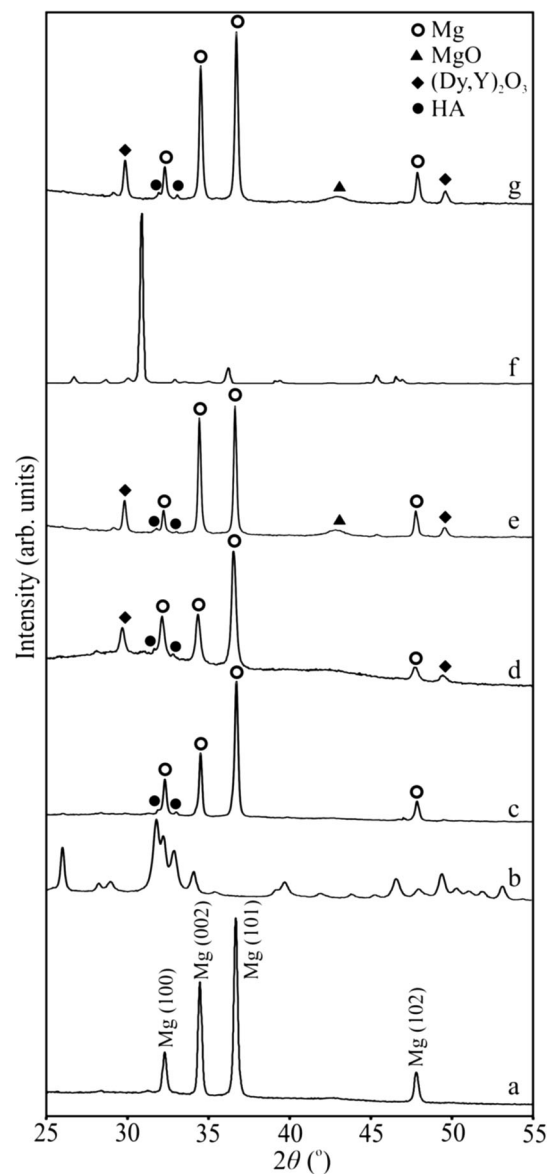


Fig. 1 XRD patterns of Mg-4Y-5.5Dy-0.5Zr and HA (5 wt.%) powders mechanically alloyed for different times: Mg-4Y-5.5Dy-0.5Zr MA for 5 min (a), HA for 0 h (b), (Mg-4Y-5.5Dy-0.5Zr)-5 wt.% HA MA for 1 h (c), (Mg-4Y-5.5Dy-0.5Zr)-5 wt.% HA MA for 25 h (d), a bulk (Mg-4Y-5.5Dy-0.5Zr)-5 wt.% HA sample after sintering under argon at $550 \text{ }^\circ\text{C}$ for 2 h (e), NH₄HCO₃ (space-holder material) (f) and (Mg-4Y-5.5Dy-0.5Zr)-5 wt.% HA scaffold with a porosity of 48% after sintering under a vacuum of 10^{-4} Torr in two steps: at $175 \text{ }^\circ\text{C}$ for 2 h and at $550 \text{ }^\circ\text{C}$ for 2 h (g)

Crystal size (d) and internal strain (ϵ) were calculated from the Mg (101) diffraction peak position. The crystal size (d) decreases rapidly during the initial stage of milling, from 340 to 60 nm (0-1 h of MA), and then begins to decrease slowly until the size of 13 nm after 25 h of mechanical alloying is reached. The ϵ increases by increasing the MA time from approximately 0.03% and reaches 0.45% after 25 h of MA. The described behavior is related to the mechanical deformation in the powder particles and is a result of the transformation of the elemental powders to the ultrafine Mg phase.

Figure 1(b) presents the XRD pattern of the hydroxyapatite. In the (Mg-4Y-5.5Dy-0.5Zr)-5 wt.% HA composition, the HA

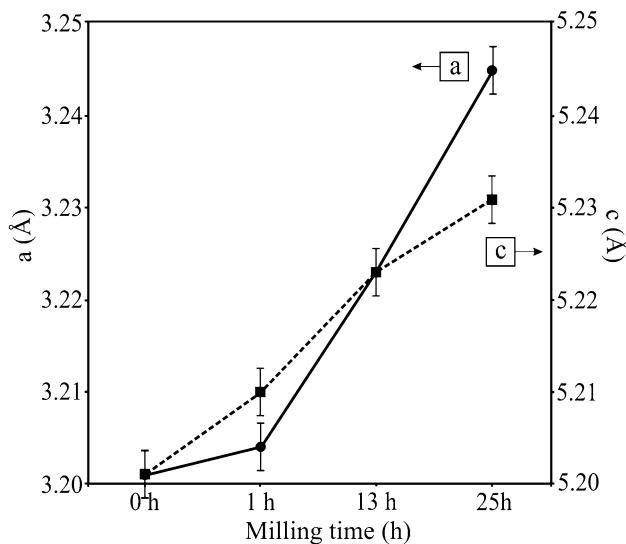


Fig. 2 Evolution of a and c lattice parameters in the Mg-4Y-5.5Dy-0.5Zr sample for different milling times

peaks almost disappeared for the sample milled for 1 h (Fig. 1c). After 25 h of MA, the Mg-RE-Zr-5 wt.% HA sample was formed by a Mg solid solution with a *cla* ratio of 1.62 (Fig. 1d). The peak positions for magnesium, the major phase, were shifted to lower angles, a shift that was consistent with the dissolved hydroxyapatite in the Mg-4Y-5.5Dy-0.5Zr matrix. The structure of this composite was formed by a fine-grained hcp α -Mg phase with the average crystallites of the size of 14 nm calculated by the Scherrer method and traces of the (Dy, Y)₂O₃ and HA phases.

Figure 3 shows the microstructure of the sintered Mg-4Y-5.5Dy-0.5Zr alloy. This material showed relatively fine grains (20–80 μ m) with second-phase particles distributed both inside the grains and on their boundaries. The precipitations are MgO and (Dy, Y)₂O₃ (point 1 on Fig. 3). The relative density of the bulk nanostructured Mg-4Y-5.5Dy-0.5Zr alloy was approx. 94.0%. The XRD analysis of the bulk (Mg-4Y-5.5Dy-0.5Zr)-5 wt.% HA composite confirmed the presence of the α -Mg-type structure with some impurities (MgO, (Dy, Y)₂O₃ and HA) (Fig. 1e).

Figure 4 shows the AFM micrographs of the Mg-4Y-5.5Dy-0.5Zr alloy (a), the (Mg-4Y-5.5Dy-0.5Zr)-5 wt.% HA (b) and (Mg-4Y-5.5Dy-0.5Zr)-10 wt.% HA (c) composites. The images confirmed the formation of agglomerates after the MA and heat treatment. The size of biggest particles observed for the Mg-4Y-5.5Dy-0.5Zr alloy equaled 90–140 nm. The sizes of the particles were larger than the size of the crystallites calculated from the Scherrer equation. The difference may result from the fact that the particles can be made up of several crystallites. The crystallites size calculated from the Scherrer equation applies only to regions with perfect crystalline order. A part of the particle volume, however, may have been composed of defective material. This part of volume is certainly not seen in the XRD data and can be seen on the AFM image. With the increase of the hydroxyapatite content in the (Mg-4Y-5.5Dy-0.5Zr)-*x* wt.% HA composite, a reduction of the grain sizes of the bulk material was noticeable (Fig. 4b, c). In the case of the bulk (Mg-4Y-5.5Dy-0.5Zr)-10 wt.% HA composite, the grain sizes of approx. 40–90 nm were recorded.

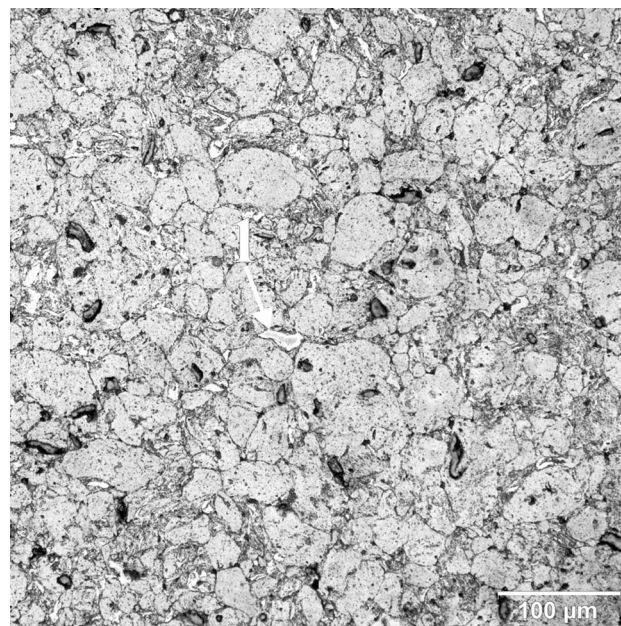


Fig. 3 Optical micrograph of a sintered bulk Mg-4Y-5.5Dy-0.5Zr sample

Based on the AFM images, particle size dimension distribution histograms for the (Mg-4Y-5.5Dy-0.5Zr)-*x* wt.% HA samples were made (Fig. 5). The size distribution of particles varied from 35 to 245 nanometers for the unmodified Mg-4Y-5.5Dy-0.5Zr alloy. The average size of the (Mg-4Y-5.5Dy-0.5Zr)-5 wt.% HA composite particles equaled 95 nm. This value is bigger than the average size of the (Mg-4Y-5.5Dy-0.5Zr)-10 wt.% HA composite particles that equaled 55 nm. Chemical modification of the Mg-4Y-5.5Dy-0.5Zr alloy by HA resulted in obtaining powder of smaller size of the particles.

The formation of the (Mg-4Y-5.5Dy-0.5Zr)-5 wt.% HA composite scaffolds was achieved by sintering under a vacuum of 10^{-4} Torr in two steps: at 175 $^{\circ}$ C for 2 h and at 550 $^{\circ}$ C for 2 h. Ammonium hydrogen carbonate was used as the spaceholder material (Fig. 1f). The XRD analysis of the (Mg-4Y-5.5Dy-0.5Zr)-5 wt.% HA scaffold with the porosity of 48% revealed the presence of an α -Mg structure with lattice parameters of $a = 3.212$ Å and $c = 5.213$ Å and MgO, (Dy, Y)₂O₃, HA (Fig. 1g). As was measured by the Scherrer formula, the crystal sizes of the bulk samples containing 0 and 5 wt.% HA were 24.6 and 25.2 nm, respectively. The scanning electron micrograph of the (Mg-4Y-5.5Dy-0.5Zr)-5 wt.% HA composite scaffold with the porosity of 48% and EDS analysis are shown in Fig. 6. This scaffold exhibited wide cavities, 100–800 μ m in diameter. Except Mg, Y, Dy, Zr, Ca, P and O were detected.

The Vickers microhardness of the sintered nanocomposites exhibited various distributions that were related to the compositional changes, and the microhardness increased with an increase in the content of hydroxyapatite. The Vickers hardnesses for the bulk Mg-4Y-5.5Dy-0.5Zr sample and the bulk (Mg-4Y-5.5Dy-0.5Zr)-5 wt.% HA nanocomposite reached 88 HV_{0.3} and 107 HV_{0.3}, respectively, and was almost twice as high as that of pure microcrystalline Mg metal (50 HV_{0.3}) (Table 1). This effect is directly associated with the transformation of the elemental powder mixtures to ultrafine particles

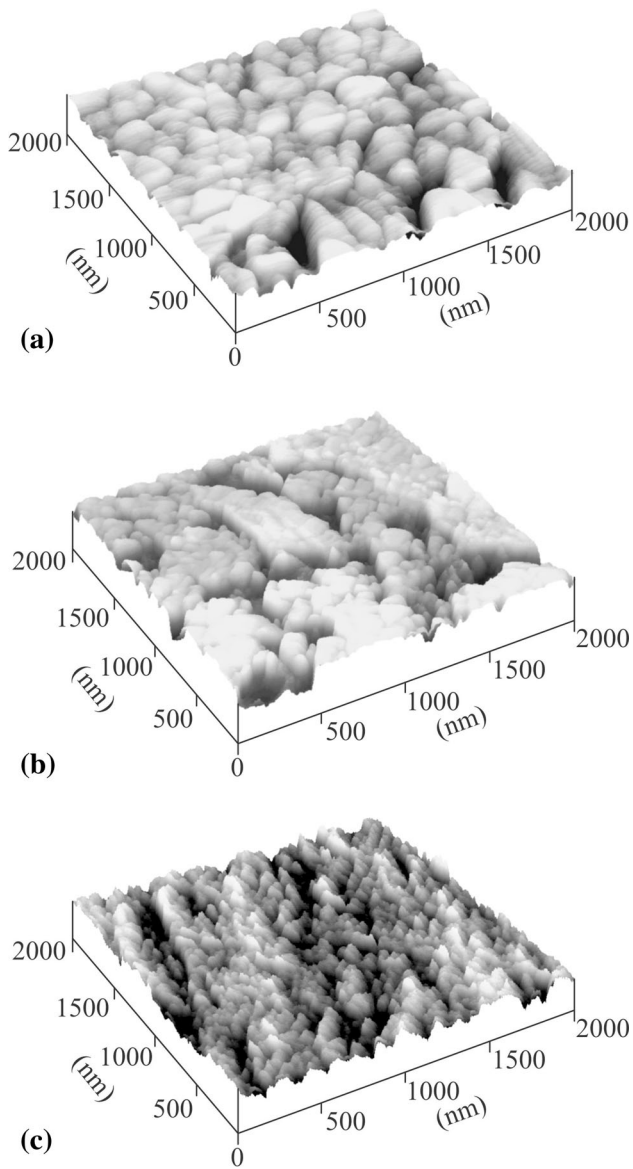


Fig. 4 AFM images of the Mg-4Y-5.5Dy-0.5Zr alloy (a), (Mg-4Y-5.5Dy-0.5Zr)-5 wt.% HA (b) and (Mg-4Y-5.5Dy-0.5Zr)-10 wt.% HA composites (c)

and the formation of defects near the surface that can act as traps for other dislocations, therefore, harden the material.

The typical room temperature engineering stress-strain curves of the Mg-4Y-5.5Dy-0.5Zr alloy (a), the (Mg-4Y-5.5Dy-0.5Zr)-5 wt.% HA composite (b) and the (Mg-4Y-5.5Dy-0.5Zr)-5 wt.% HA composite scaffold with the porosity of 48% (c) are shown in Fig. 7. The results of the measurements are listed in Table 1. Compared with the Mg-4Y-5.5Dy-0.5Zr alloy sample, the (Mg-4Y-5.5Dy-0.5Zr)-5 wt.% HA composite shows a remarkable improvement of its compressive strength. The Young's modulus (E) and the compressive strength (R_c) of the (Mg-4Y-5.5Dy-0.5Zr)-5 wt.% HA sample are 29.3 GPa and 313 MPa, respectively. In the case of the (Mg-4Y-5.5Dy-0.5Zr)-5 wt.% HA scaffolds with the porosity of 48%, the Young's modulus is equal to 7.1 GPa.

The corrosion properties were potentiodynamically investigated in the Ringer's solution at 37 °C, and the examples polarization curves are shown in Fig. 8. The nanostructured

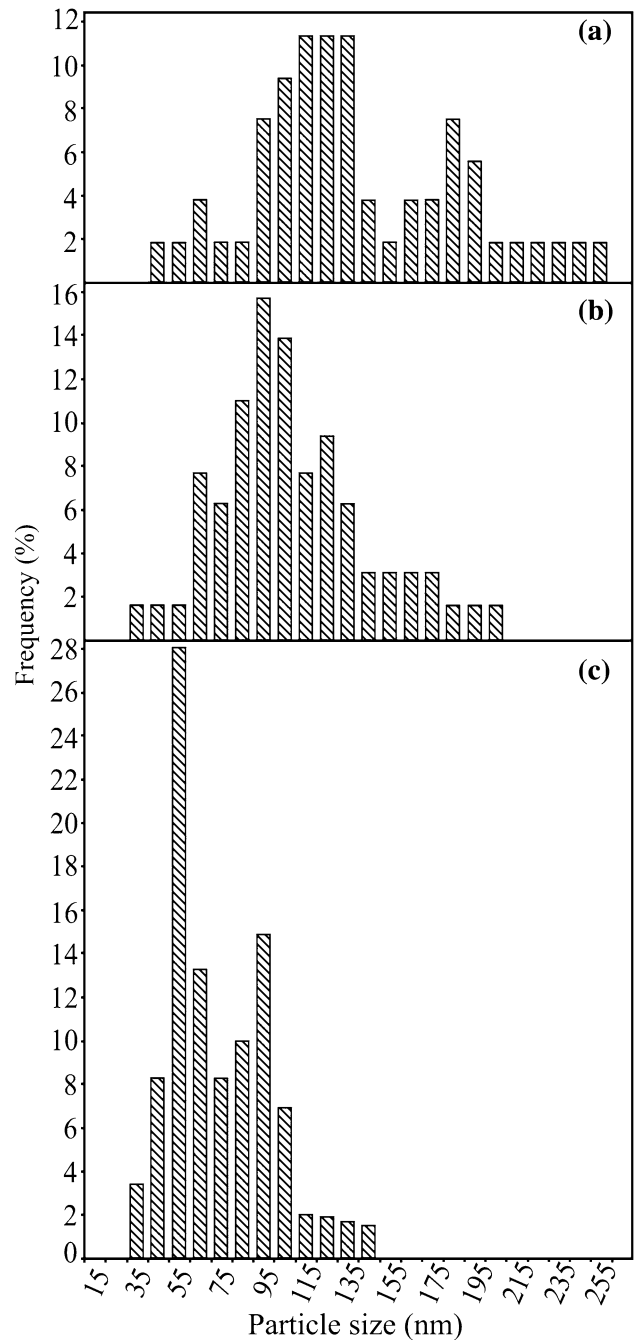


Fig. 5 Particle size dimension distribution histograms of the Mg-4Y-5.5Dy-0.5Zr alloy (a), the (Mg-4Y-5.5Dy-0.5Zr)-5 wt.% HA composite (b) and the (Mg-4Y-5.5Dy-0.5Zr)-10 wt.% HA composite (c)

(Mg-4Y-5.5Dy-0.5Zr)-10 wt.% HA composite was more corrosion resistant ($I_c = 5.849 \times 10^{-5} \text{ A cm}^{-2}$, $E_c = -1.565 \text{ V}$ versus SCE) than the Mg-4Y-5.5Dy-0.5Zr alloy ($I_c = 4.838 \times 10^{-4} \text{ A cm}^{-2}$, $E_c = -1.555 \text{ V}$ versus SCE). The lower corrosion current density indicates better corrosion resistance and lower corrosion rate. The potentiodynamic corrosion resistance tests revealed that the porosity of the (Mg-4Y-5.5Dy-0.5Zr)-5 wt.% HA nanocomposite scaffolds had no negative effects compared to the Mg-4Y-5.5Dy-0.5Zr alloy.

Independently, the influence of hydrofluoric acid treatment on the corrosion behavior of the (Mg-4Y-5.5Dy-0.5Zr)-5 wt.%

HA composites was investigated. The treatment resulted in a better protection of the substrate (Table 2). Surface treatment of the (Mg-4Y-5.5Dy-0.5Zr)-5 wt.% HA nanocomposite by immersion in 40% HF for 2 h provides a more uniform and denser MgF₂ surface layer (3 μm) compared with the untreated sample (Fig. 9b). Figure 9 shows the electrochemical polarization curves of the untreated and HF-treated bulk (Mg-4Y-

5.5Dy-0.5Zr)-5 wt.% HA composites in the Ringer's solution. The corrosion potential (E_c) of the fluoride-treated sample shifted to the nobler direction. For the 40% HF-treated specimen, the E_c was 108 mV higher than the untreated specimens. The corrosion current density (I_c) decreased from 3.630×10^{-4} to 2.518×10^{-4} A cm⁻², which shows a good corrosion resistance of the treated sample compared to the untreated one.

4. Discussion

There is a need of new generation Mg-based biomaterials for innovative implants and tissue scaffolds that would enable stimulation of the healing response of injured tissues (Ref 11, 19, 21, 22). Appropriate alloying is one of the effective measures to adjust the degradation rate as well as mechanical properties of the Mg-type alloy. Ideal biodegradable material should provide adequate mechanical fixation, complete degradation once no longer needed and complete replacement by new bone tissue.

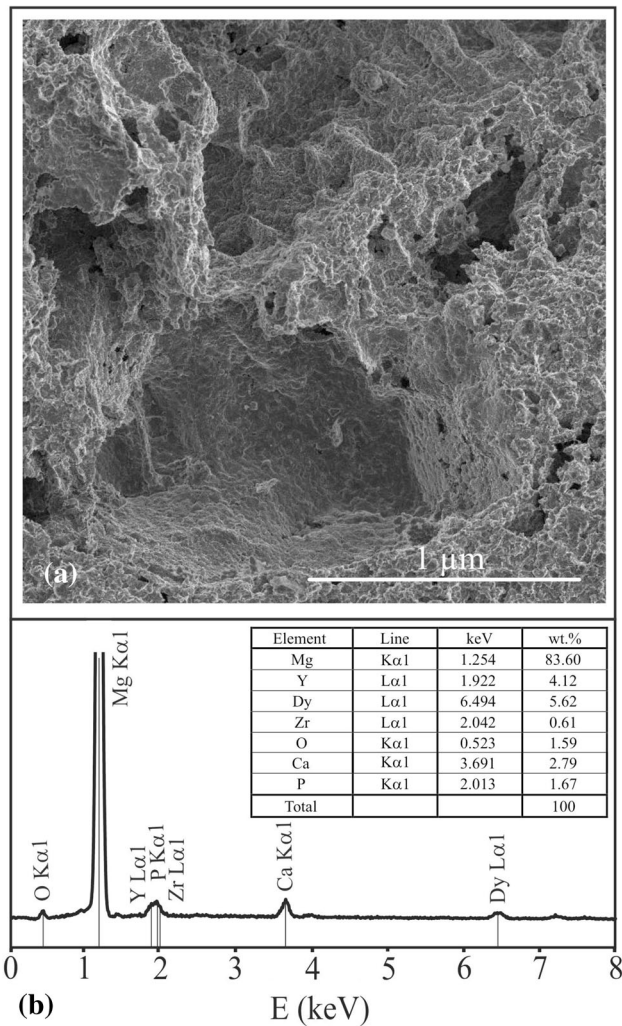


Fig. 6 SEM micrograph of the (Mg-RE-Zr)-5 wt.% HA nanocomposite scaffold with the porosity of 48% after sintering under a vacuum of 10^{-4} Torr in two steps: at 175 °C for 2 h and at 550 °C for 2 h (a) and its EDS surface spectrum (b)

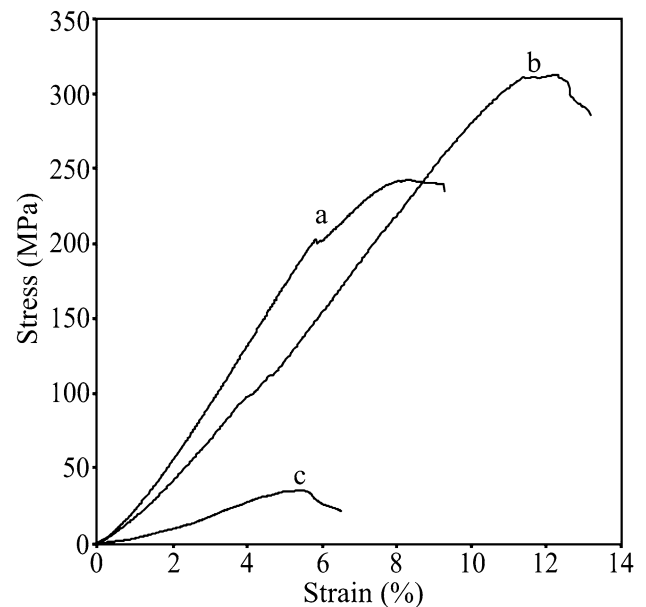


Fig. 7 Compressive stress-strain curves of the (Mg-4Y-5.5Dy-0.5Zr) alloy (a), the (Mg-4Y-5.5Dy-0.5Zr)-5 wt.% HA composite (b) and the (Mg-4Y-5.5Dy-0.5Zr)-5 wt.% HA composite scaffold with the porosity of 48% (c)

Table 1 Cell parameters (a, c), cell volume (V), theoretical density (ρ_{th}), Vickers hardness ($HV_{0.3}$), Young's modulus (E) and compressive strength (R_c) of studied bulk (Mg-4Y-5.5Dy-0.5Zr)-x wt.% HA composites and (Mg-4Y-5.5Dy-0.5Zr)-5 wt.% HA scaffold with 48% porosity in comparison with microcrystalline magnesium

Sample	a [Å]	c [Å]	V [Å ³]	ρ_{th} [g/cm ³]	$HV_{0.3}$	E [GPa]	R_c [MPa]
Bulk Mg-4Y-5.5Dy-0.5Zr	3.207	5.208	46.39	1.87	88	36.6	243±4
Bulk (Mg-4Y-5.5Dy-0.5Zr)-1 wt.% HA	3.206	5.205	46.33	1.94	102
Bulk (Mg-4Y-5.5Dy-0.5Zr)-3 wt.% HA	3.208	5.207	46.41	1.96	108
Bulk (Mg-4Y-5.5Dy-0.5Zr)-5 wt.% HA	3.207	5.206	46.37	1.98	107	29.3	313±5
Bulk (Mg-4Y-5.5Dy-0.5Zr)-10 wt.% HA	3.205	5.205	46.30	2.05	105
Scaffold (Mg-4Y-5.5Dy-0.5Zr)-5 wt.% HA with 48% porosity	3.200	5.196	46.08	7.1	35±3
Mg (microcrystalline)	3.209	5.211	46.47	1.74	50	45	198±4 (Ref 32)

Mechanical alloying is a typical top-down method for preparing nanomaterials (Ref 1). Considerable deformation during the MA process causes a large dislocation density and the formation of nanometer-sized subgrains. This technique allows alloying of elements that are difficult or impossible to combine by conventional melting methods.

The main limitation to the application of magnesium alloys as medical implant materials is their corrosion behavior. In this work, the mechanical alloying and “space-holder” sintering processes were used to synthesize bulk (Mg-4Y-5.5Dy-0.5Zr)-*x* wt.% HA samples and (Mg-4Y-5.5Dy-0.5Zr)-5 wt.% HA scaffolds. When HA is added to the Mg-4Y-5.5Dy-0.5Zr alloy, the lattice constants increase, as manifested by a shift of the diffraction peaks of the (1 0 0), (0 0 2), (1 0 1) and (102) crystal planes toward smaller angles in comparison with the Mg-4Y-5.5Dy-0.5Zr composition (Table 1).

The Young’s modulus of the (Mg-4Y-5.5Dy-0.5Zr)-5 wt.% HA scaffolds with the porosity of 48% was found to be 7.1 GPa. In terms of future application of hard tissue replacement temporary implants, a biomaterial with low elastic modulus is anticipated because the elastic modulus of natural bones is low (7-25 GPa) (Ref 6). Nanostructured biomaterials possess unique mechanical and surface properties similar to

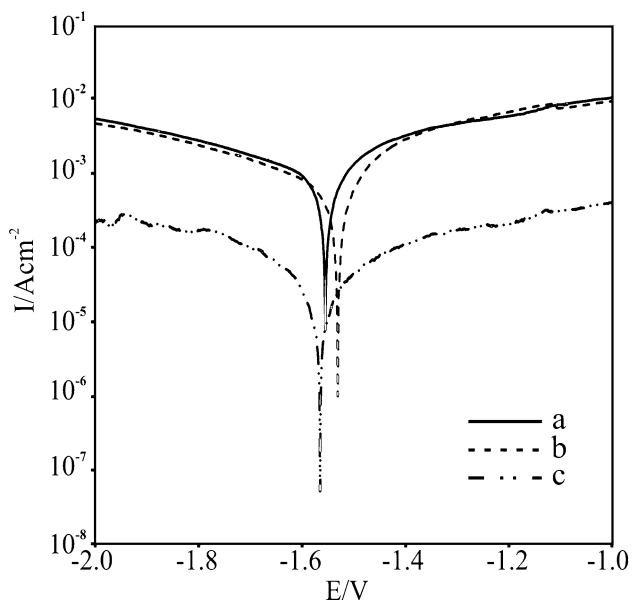


Fig. 8 Potentiodynamic polarization curves of the Mg-4Y-5.5Dy-0.5Zr alloy (a), the (Mg-4Y-5.5Dy-0.5Zr)-1 wt.% HA composite (b), the (Mg-4Y-5.5Dy-0.5Zr)-10 wt.% HA composite (c) in the Ringer’s solution at 37 °C

Table 2 Mean values of corrosion current densities (I_c) and corrosion potentials (E_c) of studied bulk (Mg-4Y-5.5Dy-0.5Zr)-*x* wt.% HA nanocomposites and bulk (Mg-4Y-5.5Dy-0.5Zr)-5 wt.% HA after immersion for 2 h in 40% HF at room temperature in comparison with microcrystalline magnesium

Sample	I_c [$A\ cm^{-2}$]	E_c versus SCE [V]
Bulk Mg-4Y-5.5Dy-0.5Zr	4.838×10^{-4}	-1.555
Bulk (Mg-4Y-5.5Dy-0.5Zr)-1 wt.% HA	8.955×10^{-4}	-1.531
Bulk (Mg-4Y-5.5Dy-0.5Zr)-3 wt.% HA	2.817×10^{-4}	-1.586
Bulk (Mg-4Y-5.5Dy-0.5Zr)-5 wt.% HA	3.630×10^{-4}	-1.551
Bulk (Mg-4Y-5.5Dy-0.5Zr)-5 wt.% HA after immersion for 2 h in 40% HF	2.518×10^{-4}	-1.443
Bulk (Mg-4Y-5.5Dy-0.5Zr)-10 wt.% HA	5.849×10^{-5}	-1.565
Mg (microcrystalline)	1.970×10^{-4}	-1.660

bone and are consequently considered to be the future generation of biomaterials (Ref 4, 5).

Hydroxyapatite is one of few materials that will support bone ingrowth and osseointegration when used in dental, orthopedic or maxillofacial applications. No decomposition of HA occurs during synthesis of the (Mg-4Y-5.5Dy-0.5Zr)-HA composites. These scaffolds will become part of the bone structure and will reduce healing times compared to a situation when no bone filler was used. Recently, Čapek and Vojtěch prepared a porous magnesium material using the powder metallurgy technique based on ammonium hydrogen carbonate as space-holder particles (Ref 23). The flexural strength of the porous Mg with the porosity of 28 vol.% was higher than the flexural strength of natural bone.

The corrosion test results indicated that the microcrystalline magnesium possesses a lower corrosion resistance and, consequently, a higher corrosion current density ($I_c = 1.97 \times 10^{-4} A\ cm^{-2}$, $E_c = -1.66 V$ versus SCE) in the Ringer’s solution. The bulk (Mg-4Y-5.5Dy-0.5Zr)-HA composites with 10 wt.% of HA have a better corrosion resistance ($I_c = 5.849 \times 10^{-5} A\ cm^{-2}$, $E_c = -1.565 V$ versus SCE). It has been suggested that rare earth elements accelerate the kinetics of the formation of MgH_2 during the corrosion process, which gradually decomposes to form $Mg(OH)_2$ in aqueous solutions, and this could act as a barrier against further corrosion of magnesium (Ref 24, 25).

The selection of the alloying elements and the control of impurity levels are the key steps toward improved corrosion resistance of magnesium alloys. For instance, the corrosion resistance of the WE43 alloy has been reported to be one hundred times better than the AZ91C and ZE41A alloys (Ref 26). Several reports have shown that decreasing the corrosion rate of Mg in simulated body fluids is possible by surface treatment methods. Among different methods, hydrofluoric acid treatment is a promising one owing to its simplicity and low cost (Ref 27, 28). By the application of the HF treatment method, the corrosion rate decreases by providing a magnesium fluoride (MgF_2) protective layer on the surface of the sample. Additionally, when the (Mg-4Y-5.5Dy-0.5Zr)-5 wt.% HA nanocomposite is immersed in 40% HF for 2 h, the protective MgF_2 layer over the surface forms (Fig. 9). On the other hand, the increased corrosion resistance is attributed to the formation of a thickened RE-oxides ($(Dy, Y)_2O_3$) layers on the surface of the synthesized (Mg-4Y-5.5Dy-0.5Zr)-*x* wt.% HA nanocomposites. The enrichment of the natural magnesium oxide film with the RE-oxides should have a beneficial effect on the corrosion resistance (Ref 19).

The surface treatment methods also include calcium phosphate coatings. For example, Hiromoto and Yamamoto synthe-

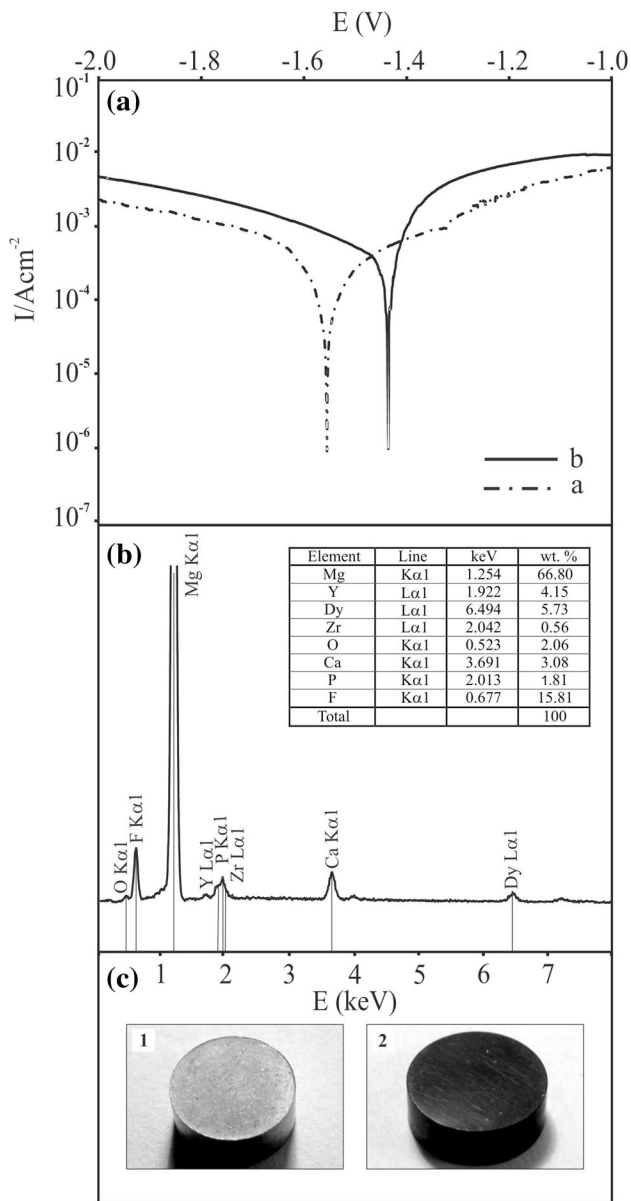


Fig. 9 Potentiodynamic polarization curves before (a) and after (b) immersion in a 40% hydrofluoric acid for 2 h at RT of the (Mg-4Y-5.5Dy-0.5Zr)-5 wt.% HA composite and EDS spectrum of the treated sample (b). Images of untreated (1) and HF-treated specimens (2) are shown in (c)

sized HA on the magnesium surface without pre-treatment by immersion in a solution of Ca-EDTA, KH_2PO_4 and NaOH at various pH values at 110 °C (Ref 29). The phase analysis of the coatings has shown that, besides HA, other phases such as magnesium hydroxide and magnesium phosphate were present. The $\text{Mg}(\text{OH})_2$ layer increased in thickness by several nanometers during immersion in water, whereas the inside MgO layer retained constant thickness. The corrosion resistance increased with a growing thickness of the coating. Thermal oxidation has also been confirmed to be a simple method of increasing the initial corrosion protection of Mg-based alloys (Ref 30). Recently, Ca-deficit hydroxyapatite coatings have been prepared on the ZK60 magnesium alloys using a biomimetic method in the SBF solutions with pH value of 5~7 and Ca/P ratio of 1.67 (Ref 31). The coatings were composed of ball-like

CaP particles with the Ca/P ratio of 0.86~1.24. The corrosion resistance and biocompatibility of the coated samples were greatly improved comparing with those of the uncoated sample. For the samples fabricated at different pH values, the sample coated from the solution with pH of 6 had the best properties for biomedical applications. Additionally, the phosphating treatment method is also a promising one to improve both the corrosion resistance and biocompatibility of the WE43 magnesium alloy (Ref 8).

5. Conclusions

Mechanical alloying and the “space-holder” sintering process were applied in order to produce the (Mg-4Y-5.5Dy-0.5Zr)-x wt.% HA composites and their scaffolds. High deformation during the MA leads to great dislocation density and formation of ultrafine grains. An improvement of the properties because of the ultrafine structure in consolidated bulk (Mg-4Y-5.5Dy-0.5Zr)-HA composites and their scaffolds has been observed.

For the bulk (Mg-4Y-5.5Dy-0.5Zr)-5 wt.% HA composite and the (Mg-4Y-5.5Dy-0.5Zr)-5 wt.% HA scaffold with the porosity of 48%, the average Young’s modulus of 29.3 GPa and 7.1 GPa was measured, respectively. By the application of the HF treatment method, the corrosion rate decreased by providing a magnesium fluoride protective layer on the surface of the (Mg-4Y-5.5Dy-0.5Zr)-HA composite samples. The bulk and porous (Mg-4Y-5.5Dy-0.5Zr)-HA composites would offer new structural and functional properties for innovative products in medical applications.

Acknowledgments

The work has been financed by National Science Centre Poland under the Decision No. DEC-2013/11/B/ST8/04394.

Open Access

This article is distributed under the terms of the Creative Commons Attribution 4.0 International License (<http://creativecommons.org/licenses/by/4.0/>), which permits unrestricted use, distribution, and reproduction in any medium, provided you give appropriate credit to the original author(s) and the source, provide a link to the Creative Commons license, and indicate if changes were made.

References

1. J.S. Benjamin, Mechanical Alloying, *Sci. Am.*, 1976, **234**, p 40–46
2. S.M. Fatemi-Varzaneh, A. Zarei-Hanzaki, and H. Paul, Characterization of Ultrafine and Nano Grained Magnesium Alloy Processed by Severe Plastic Deformation, *Mater. Charact.*, 2014, **87**, p 27–35
3. K. Niespodziana, K. Jurczyk, J. Jakubowicz, and M. Jurczyk, Fabrication and Properties of Titanium-Hydroxyapatite Nanocomposites, *Mater. Chem. Phys.*, 2010, **123**, p 160–165
4. B.C. Ward and T.J. Webster, INCREASED Functions of Osteoblasts on Nanophase Metals, *Mater. Sci. Eng. C*, 2007, **27**, p 575–578
5. M. Kaczmarek, M.U. Jurczyk, B. Rubis, A. Banaszak, A. Kolecka, A. Paszel, K. Jurczyk, M. Murias, J. Sikora, and M. Jurczyk, In Vitro Biocompatibility of Ti-45S5 Bioglass Nanocomposites and Their Scaffolds, *J. Biomed. Mater. Res. A*, 2014, **102**(5), p 1316–1324

6. N. Li and Y. Zheng, Novel Magnesium Alloys Developed for Biomedical Application: A Review, *J. Mater. Sci. Technol.*, 2013, **29**(6), p 489–502
7. N. Li, C. Guo, Y.H. Wu, Y.F. Zheng, and L.Q. Ruan, Comparative Study on Corrosion Behaviour of Pure Mg and WE43 Alloy in Static, Stirring and Flowing Hank's Solution, *Corros. Eng. Sci. TechOL.*, 2012, **47**(5), p 346–351
8. C.H. Ye, T.F. Xi, Y.F. Zheng, S.Q. Wang, and Y.D. Li, In Vitro Corrosion and Biocompatibility of Phosphating Modified WE43 Magnesium Alloy, *Trans. Nonferrous Met. Soc. China*, 2013, **23**(4), p 996–1001
9. G. Song, Recent Progress in Corrosion and Protection of Magnesium Alloys, *Adv. Eng. Mater.*, 2005, **7**(7), p 563–586
10. R.C. Zeng, J. Zhang, W.J. Huang, W. Dietzel, K.U. Kainer, C. Blawert, and W. Ke, Review of Studies on Corrosion of Magnesium Alloys, *Trans. Nonferrous Met. Soc. China*, 2006, **16**(2), p 763–771
11. F. Witte, The History of Biodegradable Magnesium Implants: A Review, *Acta Biomater.*, 2010, **6**(5), p 1680–1692
12. F. Zucchi, V. Grassi, A. Frignani, C. Monticelli, and G. Trabaneli, Electrochemical Behaviour of a Magnesium Alloy Containing Rare Earth Elements, *J. Appl. Electrochem.*, 2006, **36**(2), p 195–204
13. Electron WE43—datasheet: 467, Magnesium Electron Products, Manchester, England
14. I. Nakatsugawa, S. Kamado, Y. Kojima, R. Ninomiya, and K. Kubota, Corrosion of Magnesium Alloys Containing Rare Earth Elements, *Corros. Rev.*, 1998, **16**(1–2), p 139–157
15. K.A. Khalil, A New-Developed Nanostructured Mg/HAP Nanocomposite by High Frequency Induction Heat Sintering Process, *Int. J. Electrochem. Sci.*, 2012, **7**(11), p 10698–10710
16. F. Witte, F. Feyerabend, P. Maier, J. Fischer, M. Störmer, C. Blawert, W. Dietzel, and N. Hort, Biodegradable Magnesium-Hydroxyapatite Metal Matrix Composites, *Biomaterials*, 2007, **28**(13), p 2163–2174
17. M. Tulinski and M. Jurczyk, Nanostructured Nickel-Free Austenitic Stainless Steel Composites with Different Content of Hydroxyapatite, *Appl. Surface Sci.*, 2012, **260**, p 80–83
18. A.K. Khanra, H.C. Jung, S.H. Yu, K.S. Hong, and K.S. Shin, Microstructure and Mechanical Properties of Mg-HAP Composites, *Bull. Mater. Sci.*, 2010, **33**(1), p 43–47
19. Y.F. Zheng, X.N. Gu, and F. Witte, Biodegradable Metals, *Mater. Sci. Eng. R*, 2014, **77**, p 1–34
20. K. Bobe, E. Willbold, I. Morgenthal, O. Andersen, T. Studnitzky, J. Nellesen, W. Tillmann, C. Vogt, K. Vano, and F. Witte, In Vitro and in Vivo Evaluation of Biodegradable, open-Porous Scaffolds Made of Sintered Magnesium W4 Short Fibres, *Acta Biomater.*, 2013, **9**(10), p 8611–8623
21. F. Witte, N. Hort, C. Vogt, S. Cohen, K.U. Kainer, and R. Willumeit, Degradable Biomaterials Based on Magnesium Corrosion, *J. Curr. Opin. Solid State Mater. Sci.*, 2008, **12**(5–6), p 63–72
22. D. Bellucci, V. Cannillo, A. Cattini, and A. Sola, A New Generation of Scaffolds for Bone Tissue Engineering, *Ind. Ceram.*, 2011, **31**(1), p 59–62
23. J. Capek and D. Vojtěch, Properties of Porous Magnesium Prepared by Powder Metallurgy, *Mater. Sci. Eng. C*, 2013, **33**(1), p 564–569
24. R. Arrabal, E. Matykina, F. Viejo, P. Skeldon, and G.E. Thompson, Corrosion Resistance of WE43 and AZ91D Magnesium Alloys with Phosphate PEO Coatings, *Corros. Sci.*, 2008, **50**, p 1744–1752
25. H. Hornberger, S. Virtanen, and A.R. Boccaccini, Biomedical Coatings on Magnesium Alloys—A Review, *Acta Biomater.*, 2012, **8**(7), p 2442–2455
26. G. Song, A. Atrens, X. Wu, and B. Zhang, Corrosion Behaviour of AZ21, AZ501 and AZ91 in Sodium Chloride, *Corros. Sci.*, 1998, **40**(10), p 1769–1791
27. E.C. Meng, S.K. Guan, H.X. Wang, L.G. Wang, S.J. Zhu, J.H. Hu, C.X. Ren, J.H. Gao, and Y.S. Feng, *Appl. Sur. Sci.*, 2011, **257**, p 4811–4816
28. M. Razavi, M.H. Fathi, and M. Meratian, Fabrication and Characterization of Magnesium-Fluorapatite Nanocomposite for Biomedical Applications, *Mater. Charact.*, 2010, **61**(12), p 1363–1370
29. S. Hiromoto and A. Yamamoto, High Corrosion Resistance of Magnesium Coated with Hydroxyapatite Directly Synthesized in an Aqueous Solution, *Electrochim. Acta*, 2009, **54**(27), p 7085–7093
30. A.C. Hänzli, P. Gunde, M. Schinhammer, and P.J. Uggowitzer, On the Biodegradation Performance of an Mg-Y-RE Alloy with Various Surface Conditions in Simulated Body Fluid, *Acta Biomater.*, 2009, **5**(1), p 162–171
31. W. Lu, Z. Chen, P. Huang, and B. Yan, Microstructure, Corrosion Resistance and Biocompatibility of Biomimetic HA-Based Ca-P Coatings on ZK60 Magnesium Alloy, *Int. J. Electrochem. Sci.*, 2012, **7**(12), p 12668–12679
32. Y. Wan, G. Xiong, H. Luo, F. He, Y. Huang, and X. Zhou, Preparation and Characterization of a New Biomedical Magnesium-Calcium Alloy, *Mater. Design*, 2008, **29**(10), p 2034–2037